Supporting Information for

The organic-moiety-dominated Li^+ intercalation/deintercalation mechanism of a cobalt-based metal-organic framework

Chao Li,[a] Xiaoshi Hu,[a] Xiaobing Lou,[a] Lijuan Zhang,[b] Yong Wang,[b] Jean-Paul Amoureux,[a] Ming Shen,[a,*] Qun Chen,[a] and Bingwen Hu[a,*]

[a]*State Key Laboratory of Precision Spectroscopy, Shanghai Key Laboratory of Magnetic Resonance, Institute of Functional Materials, School of Physics and Materials Science, East China Normal University, Shanghai 200062, P.R. China.*

[b]*Shanghai Synchrotron Radiation Facility (SSRF), Shanghai 201204, P.R. China.*

Corresponding Author:

*(M.S.) E-mail: mshen@phy.ecnu.edu.cn.

*(B.H.) E-mail: bwhu@phy.ecnu.edu.cn.

Table of contents.

Experimental details

Synthesis of S-Co-MOF. All chemicals and solvents were purchased from commercial suppliers and used as received. The S-Co-MOF was synthesized by a surfactant-assisted solvothermal reaction. Typically, A solution of $Co(NO_3)_2 \cdot 6H_2O$ (1.717 mmol, 0.5 g) in 20 mL deionized water was added to a solution of 1,4-benzenedicarboxylic acid (H_2BDC) (0.859 mmol, 0.143 g) in 40 mL dimethyl formamide/ethanol (1:1 vol%) and mixed to obtain a stable solution, 0.5 g polyvinylpyrrolidone (PVP) was added as the surfactant for the vertical growth of S-Co-MOF. The resulting solution was then transferred into a 100 mL Teflon-lined high pressure autoclave. After sealing, the autoclave was heated to 110 °C for 60 h and cooled down to room temperature naturally. Finally, the resultant precipitate was collected by suction filtration and rinsed with dimethyl formamide and ethanol for several times to remove the residue starting material, followed by vacuum desiccation at 110 °C for 12 h.

Characterization of S-Co-MOF. Powder X-ray diffraction (PXRD) patterns were collected on a Holland Panalytical PRO PW3040/60 Diffractometer with high-density Cu-Kα radiation (λ=1.5418 Å). Scanning electron microscope (SEM) images were taken on an S-4800 (HITACHI, Japan) operating at 10 kV, 100 μA. Transmission electron microscopy (TEM) was carried out on a JEM-2100F (JEOL Ltd., Japan) operating at 10 kV in scanning TEM mode. Fourier-transform infrared (FT-IR) spectra were recorded on a Nicolet-Nexus 670 infrared spectrometer in the form of KBr pellets. Thermogravimetric analysis (TGA) was performed on a STA 449 F3

Jupiter® simultaneous thermo-analyzer under N_2 atmosphere from 25 °C to 800 °C at a heating rate 10 °C/min. X-ray photoelectron spectroscopy (XPS) was recorded on a AXIS Ultra DLD spectrometer (SHIMADZU Ltd., Japan) operating at 250 W. N_2 sorption isotherm was measured at 77 K with an ASAP 2020 Accelerated Surface Area and Porosimetry System (Microeritics, Norcross, GA), Brunauer-Emmett-Teller (BET) and Barrett-Joyner-Halenda (BJH) analyses were used to calculate the specific surface area, and the corresponding pore size distribution.

Electrochemical Measurements. The electrochemical behavior of the S-Co-MOF was examined by using CR2032 coin-type cells with lithium foil (diameter of 14.0 mm) as the counter/reference electrode, a Celgard 2325 membrane (diameter of 19.0 mm) as the separator, and 1 M $LiPF_6$ in ethylene carbonate (EC)/ diethyl carbonate (DEC)/ dimethyl carbonate (DMC) (1:1:1 vol %) containing 5 wt% fluoroethylene carbonate (FEC) as the electrolyte. The working electrode was prepared by coating a mixture containing 70 wt% active material (S-Co-MOF), 20 wt% acetylene black, and 10 wt% carboxymethyl cellulose (CMC) onto a copper foil substrate and then drying in vacuum at 110 °C for 4 h. The mass loading of active materials on the substrate was ~2.0 mg cm^{-2}. All the cells were assembled in an argon-filled glovebox and tested at 25 °C. All the specific capacities are calculated based on the mass of S-Co-MOF. Cyclic voltammogram (CV) and electrochemical impedance spectroscopy (EIS) measurements were conducted on a CHI 660a electrochemical workstation (ChenHua Instruments Co., China). Galvanostatic charge/discharge performance was recorded

between 0.01 and 3 V (vs. Li/Li^+) using a multichannel LAND CT2001A cycler (Wuhan Kingnuo Electronic Co., China).

sXAS characterization. Soft X-ray absorption spectroscopy (sXAS) was performed at Shanghai Synchrotron Radiation Facility (SSRF, BL08U1A). Total electron yield (TEY) spectra were recorded by detecting the electric current caused by excited electrons from the S-Co-MOF electrodes, which required halting the electrochemical cycling intermittently. The battery cells were firstly cycled to the desired states-of-charge (SOC) at a current density of 100 mA g^{-1} and then disassembled in an argon-filled glovebox, and the S-Co-MOF electrodes were subsequently drawn out from the cells. The S-Co-MOF electrodes were first rinsed triple with 3 mL anhydrous DMC and then soaked in 5 ml anhydrous DMC for 12 h. The solvent was decanted and the wet electrodes were dried for 12 h at room temperature in the argon-filled glovebox. All S-Co-MOF electrode preparations were conducted in inert atmosphere, except during the insertion to the sXAS chamber, when the electrodes were exposed to air for only a few minutes.

NMR characterization. The battery cells were firstly cycled to the desired states-of-charge (SOC) at a current density of 100 mA g^{-1} and then rested for more than 12 h before collecting the electrode materials for ex-situ NMR tests. The retrieved materials were first washed triple with 3 mL anhydrous DMC and then soaked in 5 ml anhydrous DMC for 12 h. The solvent was decanted and the wet materials were dried for 12 h at room temperature in the argon-filled glovebox. Solid-state NMR (ssNMR) measurements were performed by a Bruker Avance III spectrometer equipped with a

14.10 T widebore supercoducting magnet, at Larmor frequency of 150.9 MHz for ^{13}C. Samples were packed into commercial Bruker 1.3 mm ZrO_2 rotors and rotated at a magic-angle spinning (MAS) rate of ~60 kHz using a triple-resonance 1.3 mm MAS probe. The ^{13}C MAS spectra were acquired using a rotor-synchronized spin echo pulse sequence, with typical τ duration of one rotor period (~16.67 μs), and a recycle interval of 20 ms, and the chemical shifts were referenced to the high-frequency peak of an external sample of adamantane at 38.56 ppm.

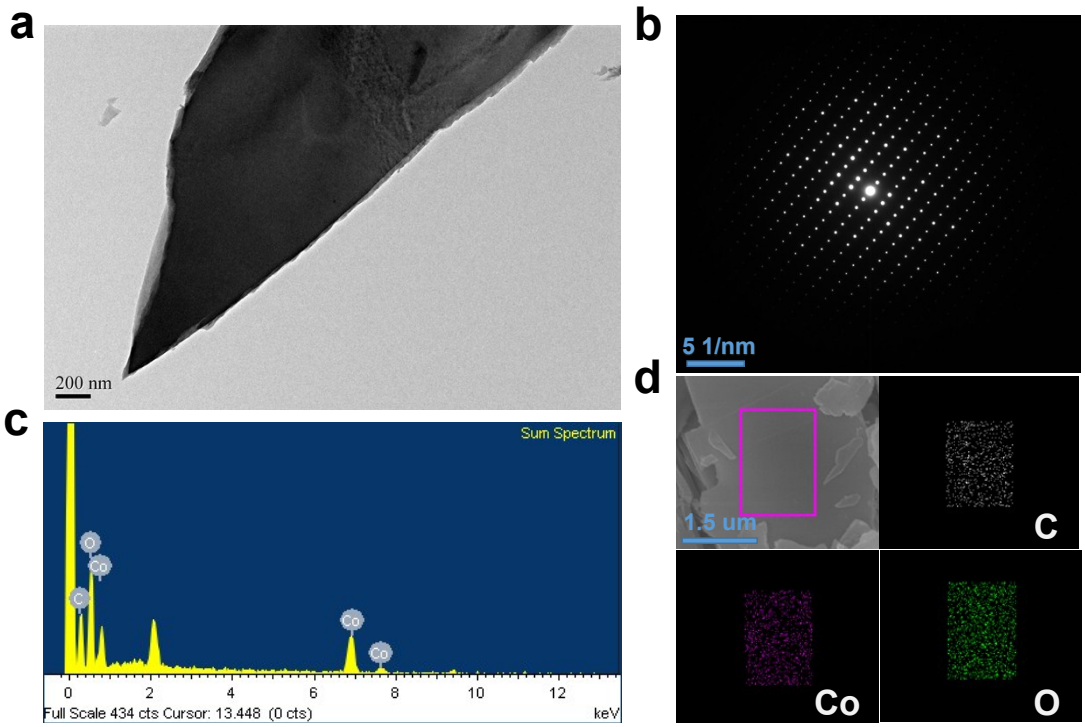

Figure S1. TEM micrograph (a) and the corresponding SAED patterns (b) of the as-synthesized S-Co-MOF. The uniform-contrast TEM image of S-Co-MOF clearly demonstrates its solid and dense nature without discernible porosity. EDX spectrum (c) and elemental mapping images (d) of S-Co-MOF from selected region, from which the coexistence and homogeneous distribution of C, O, and Co elements within the S-Co-MOF lamella are determined.

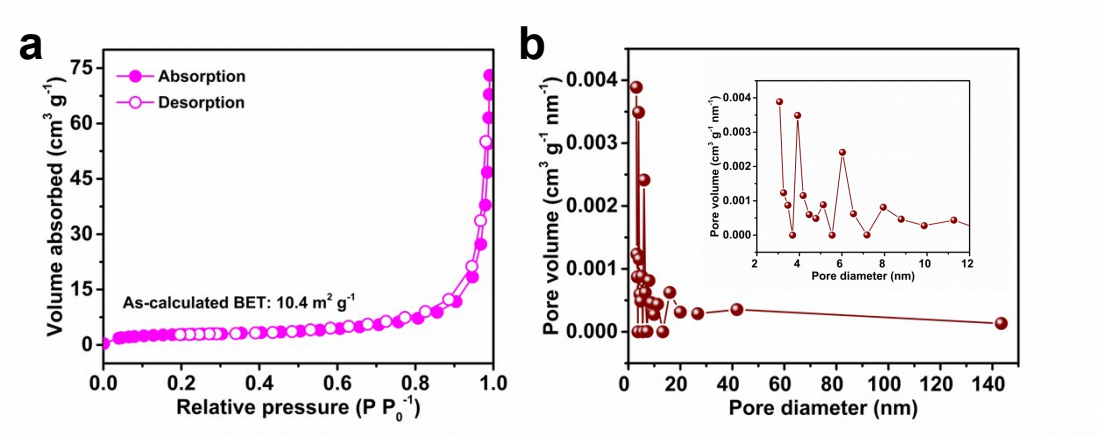

Figure S2. (a) N_2 adsorption-desorption isotherms and (b) the corresponding BJH pore size distribution of the S-Co-MOF.

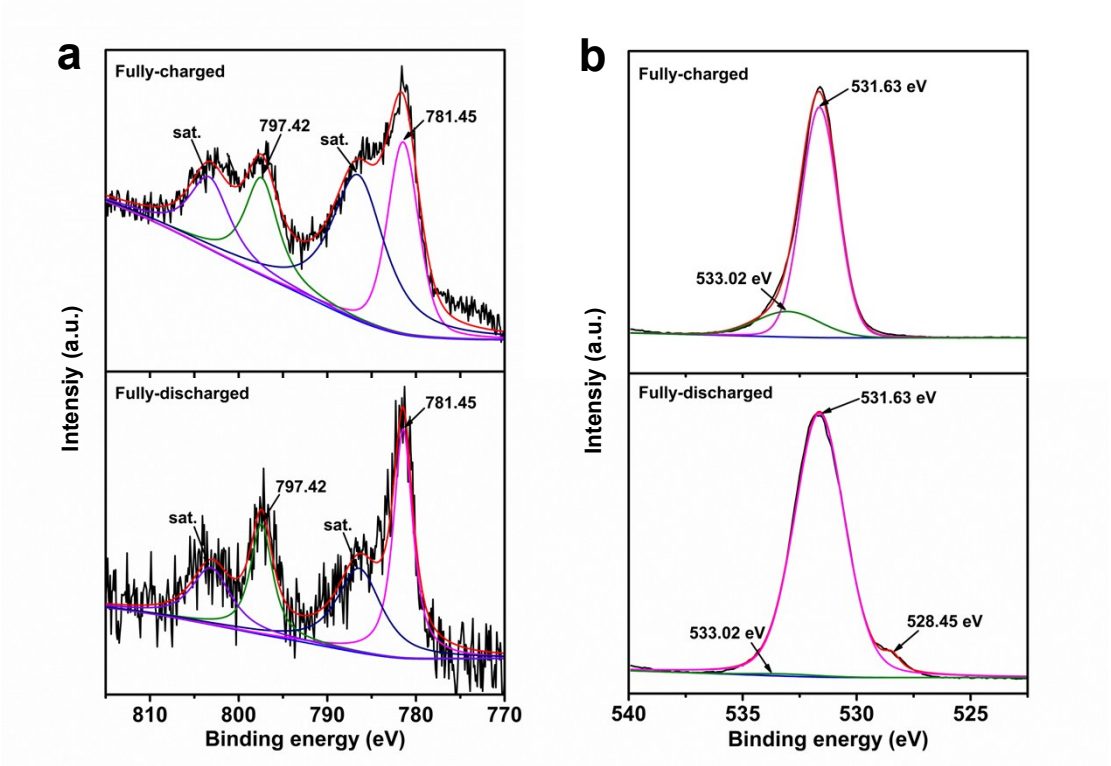

Figure S3. (a) High-resolution Co 2p and (b) O 1s XPS spectra of the fully-discharged (0.01 V) and fully-charged (3.0 V) S-Co-MOF electrodes. The nearly unchanged binding energy positions of the peaks in Figure S3a compared with the pristine sample (Figure 2a) confirm the similar Co electrical states on the electrode surface during discharge/charge process. Besides, O 1s XPS signals belonging to the normal Co-O coordination bonds (531.63 eV) and the hydroxyl group (533.02 eV) are clearly defined in Figure S3b, and a new specific peak at ~528.45 eV is observed for the fully-discharged electrode, which should be related with Li-ions intercalation to the carboxyl groups from BDC^{2-} ligand.

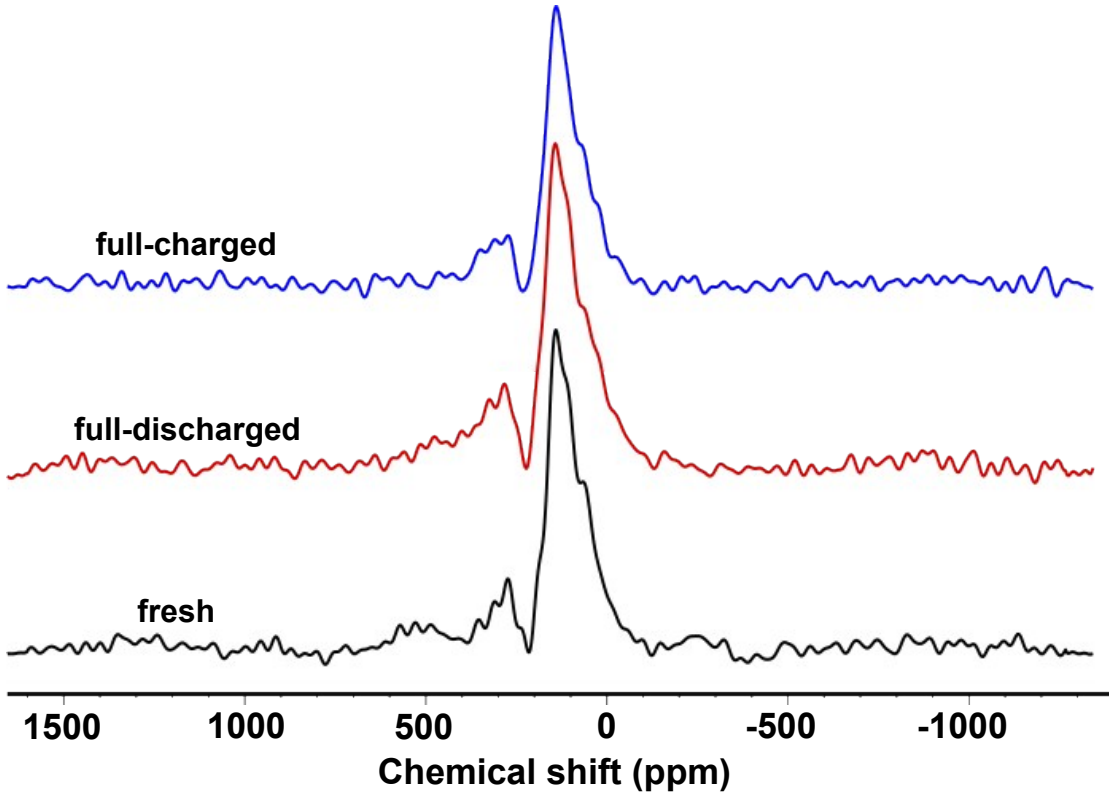

Figure S4. ^{13}C MAS NMR spectra of the DMC-washed S-Co-MOF electrode materials at the fresh, full-discharged and full-charged state. The ^{13}C spectral peaks of S-Co-MOF are located in the range of 400 to -100 ppm, the peaks in the region of 387-217 ppm can be assigned to the carboxyl groups, whereas the peaks in the region of 217 to -120 ppm can be ascribed to the ^{13}C from benzene rings.

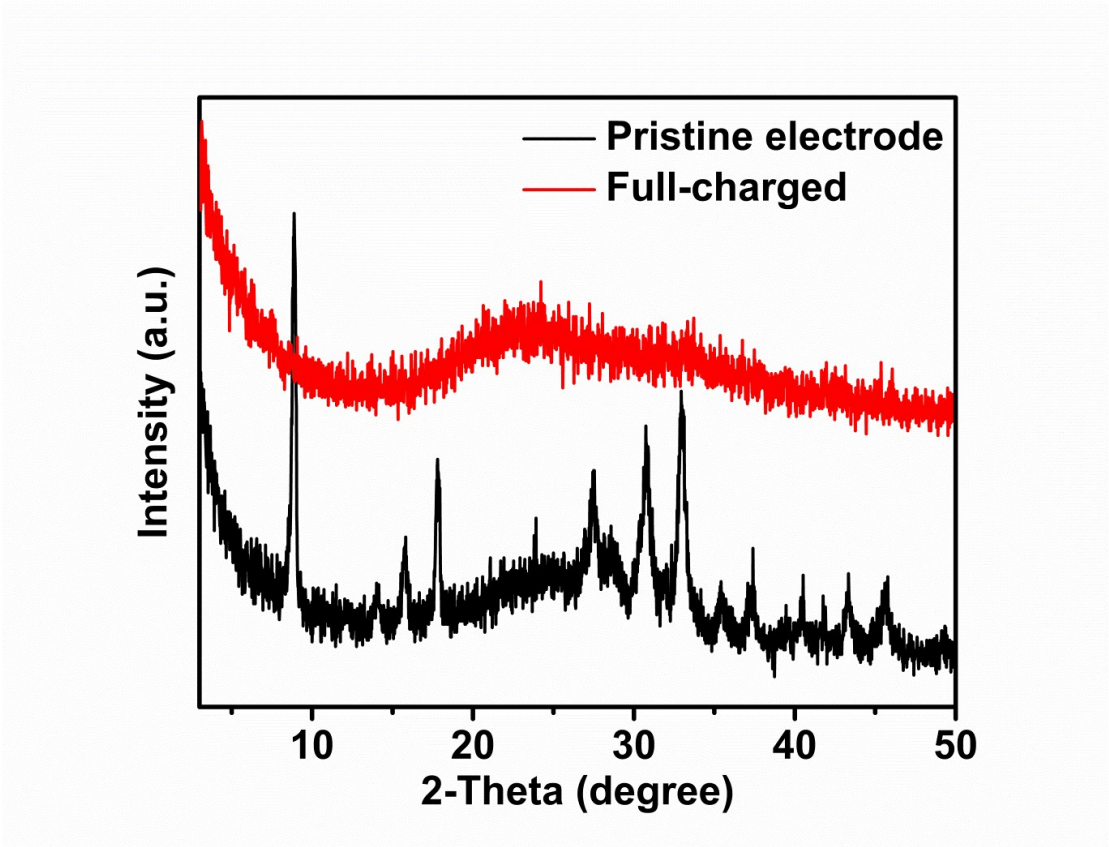

Figure S5. PXRD patterns of the fully-charged S-Co-MOF electrode and the patterns of the pristine S-Co-MOF electrode.

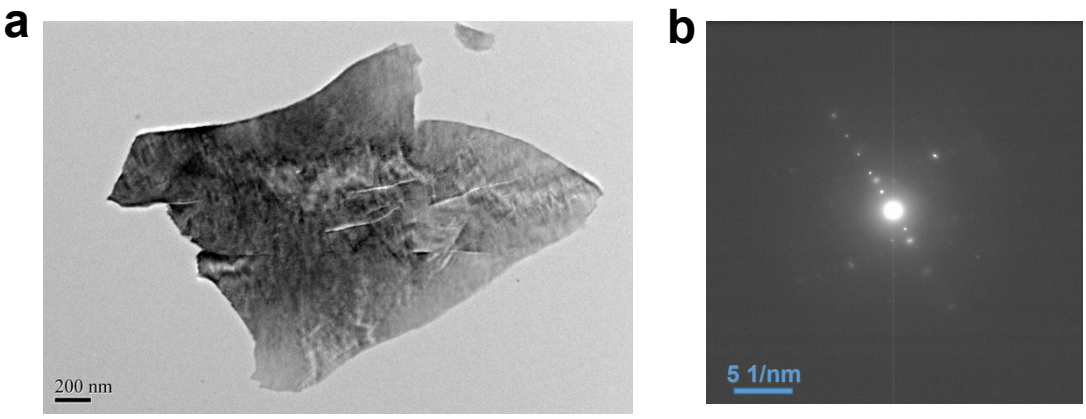

Figure S6. (a) TEM micrograph and (b) the corresponding SAED patterns of the fully-charged (3.0 V) S-Co-MOF electrode materials. The corresponding SAED patterns show that the fully-charged S-Co-MOF is nearly amorphous with a small amount of crystallites, which coincides well with the corresponding PXRD patterns in Figure S5.

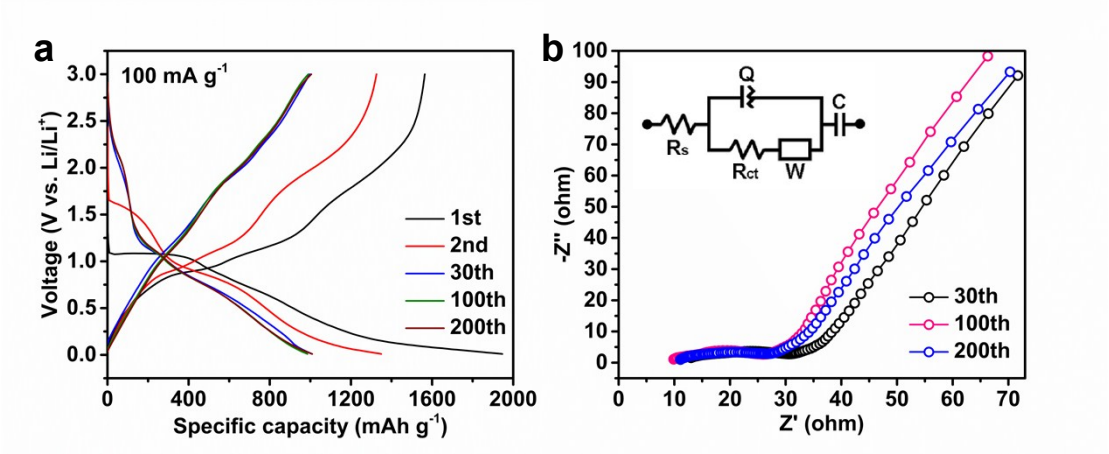

Figure S7. (a) Representive galvanostatic charge-discharge profiles for S-Co-MOF at a current density of 100 mA g^{-1}. The galvanostatic lithiation voltage profile presents a higher voltage plateau at ≈1.1 V for the first Li^+ intercalation process, which can be ascribed to the SEI formation and some side reactions with S-Co-MOF; while this is not visible for the following cycles. A long sloping lower voltage plateau is observed during which most Li^+ is intercalated into the carboxyl groups and benzene rings of S-Co-MOF. In comparison, during delithiation the voltage pattern shows a more continuous increase from 0.01 V to the cut-off voltage. The charge-discharge profile for the 2nd cycle is much different from that of the 30th, indicating some activation and stabilization processes for the S-Co-MOF electrode. Moreover, the discharge and charge profiles for S-Co-MOF are similar from the 30th cycle to 200th cycle, indicating that similar redox reactions are occurring during the charging/discharging processes as well as the stable of the S-Co-MOF electrode after the activation and stabilization processes. The feature at ~2V is also observed in other MOFs-based systems, [S1, S2] which could be ascribed to the Li-ions intercalation process into the void space of the S-Co-MOF structure (as analyzed in next page). (b) EIS spectra for

the S-Co-MOF electrode after different numbers of cycles. It can be observed that the R_{SEI} and R_{ct} for the S-Co-MOF electrode are relatively small and nearly unchanged with cycling, which demonstrates the superb cycling performance of S-Co-MOF as well as indicates a fast solid-state Li^+ diffusion rate and limited growth of SEI layers during the cycling process.

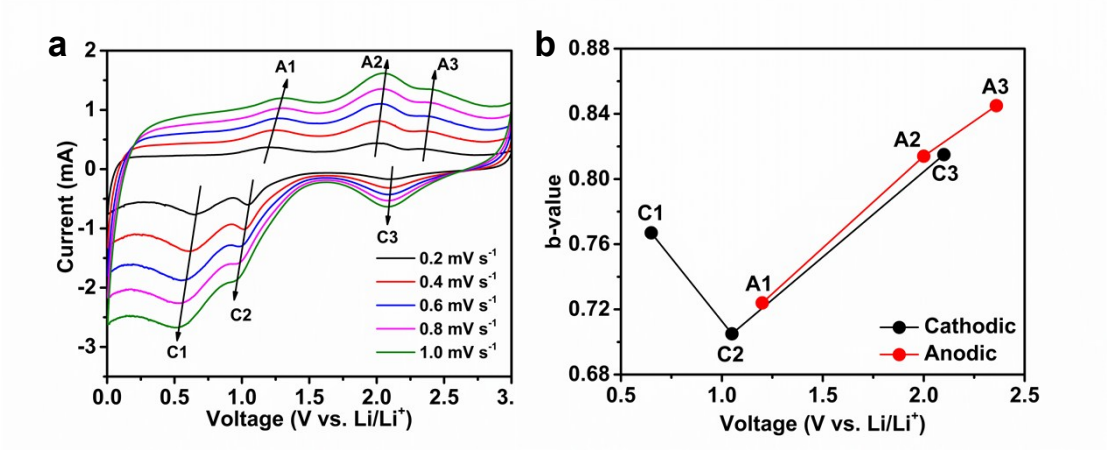

Figure S8. (a) Typical CV curves at various sweep rates and (b) calculated *b*-values as a function of voltage for cathodic and anodic scans for the S-Co-MOF electrode.

The total capacity of an electrode can be separated into three parts: the faradaic contribution caused by the Li^+ insertion/extraction reaction, the faradaic contribution from the charge transfer with surface atoms on the surface, and the nonfaradaic contribution from the double-layer effect. The latter two parts cannot be separated and could be called as capacitive effect, while the first part could be called as battery

effect. The capacitive or battery effect of the battery system is calculated according to Equations as follows:

$$i(V) = av^b \quad (1)$$

$$\lg i(V) = b \lg v + \lg a \quad (2)$$

Where *i(V)* is the measured current, *υ* is scan rate, *a* and *b* are adjustable parameters. As reported by previous works, the electrode is controlled by the Li^+ insertion/extraction process when the *b*-value is ~0.5, while a capacitive effect is dominant when the *b*-value is ~1.0.[S3, S4] In our case, the *b*-values are in the range of 0.72-0.82 for the cathodic process and 0.72-0.85 for the anodic process, which suggest that both the capacitive and battery effects contribute to the total capacity. Moreover, it is noteworthy to mention in both cathodic process and anodic process, the Li^+ insertion/extraction dominates the process around 1.1 V while the capacitive effect dominates the process around 2.1 V.

Table S1. Metal organic frameworks-based anode materials in Li-ion batteries

MOFs	Voltage window (V vs. Li/Li^+)	Current rate (mA g^{-1})	Initial Coulombic efficiency	Capacity retention (mAh g^{-1})	Cycle number	Refs.
Zn_4O(1,3,5-benzenetribenzoates)	0.05-1.6	50	~28.2%	105	50	S5
Li/Ni-1,4,5,8-naphthalenetetracarboxylates	0.01-3.0	100	55.4%	475	80	S6
Mn(tfbdc)(4,4'-bpy)$(H_2O)_2$)	0.01-2.5	50	~33.2%	390	50	S7
$[Li_6(pda)_3]$·2EtOH	0.2-2.0	30	34.2%	160	50	S8
Ni-Me_4bpz	0.01-3.0	50	43.8%	120	100	S9
$Zn(IM)_{1.5}(abIM)_{0.5}$	0.01-3.0	100, 400	51% (100 mA g^{-1})	190, 75	200, 200	S10
Mn-BTC	0.01-2.0	103, 1030	~41% (103 mA g^{-1})	694, 400	100, 100	S2
Co 2,5-furandicarboxylate	0.01-3.0	100, 1250	~71% (100 mA g^{-1})	549.8, 513.4	95, 499	S11
Mn 2,5-thiophenedicarboxylate	0.01-3.0	400	~37%	647.5	250	S12
Cu-BTC	0.05-3.0	96, 383	~44% (103 mA g^{-1})	740, 474	50, 50	S13
CoBTC-EtOH	0.01-3.0	100, 2000	49.2% (100 mA g^{-1})	856, 473	100, 500	S1
Co(tfbdc)(4,4'-bpy)$(H_2O)_2$	0.01-3.0	50	~37% (50 mA g^{-1})	545	50	S14
S-Co-MOF	0.01-3.0	100, 500, 1000	80.4% (100 mA g^{-1})	1021, 601, 435	200, 700, 1000	This work

Supplementary References

S1 C. Li, X. Lou, M. Shen, X. Hu, Z. Guo, Y. Wang, B. Hu and Q. Chen, *ACS Appl. Mater. Inter.,* 2016, **8**, 15352−15360.

S2 S. Maiti, A. Pramanik, U. Manju and S. Mahanty, *ACS Appl. Mater. Inter.*, 2015, **7**, 16357-16363.

S3 Z. Hu, L. Wang, K. Zhang, J. Wang, F. Cheng, Z. Tao and J. Chen, *Angew. Chem. Int. Ed.*, 2014, **53**, 12794-12798.

S4 K. Cao, L. Jiao, Y. Liu, H. Liu, Y. Wang and H. Yuan, *Adv. Funct. Mater.*, 2015, **25**, 1082-1089.

S5 X. Li, F. Cheng, S. Zhang and J. Chen, *J. Power Sources*, 2006, **160**, 542-547.

S6 X. Han, F. Yi, T. Sun and J. Sun, *Electrochem. Commun.*, 2012, **25**, 136-139.

S7 Q. Liu, L. Yu, Y. Wang, Y. Ji, J. Horvat, M. Cheng, X. Jia and G. Wang, *Inorg. Chem.*, 2013, **52**, 2817-2822.

S8 L. Gou, H. Zhang, X. Fan and D. Li, *Inorg. Chim. Acta*, 2013, **394**, 10-14.

S9 T. An, Y. Wang, J. Tang, Y. Wang, L. Zhang and G. Zheng, *J. Colloid Interf. Sci.*, 2015, **445**, 320-325.

S10 Y. Lin, Q. Zhang, C. Zhao, H. Li, C. Kong, C. Shen and L. Chen, *Chem. Commun.*, 2015, **51**, 697-699.

S11 H. Fei, X. Liu and Z. Li, *Chem. Eng. J.*, 2015, **281**, 453-458.

S12 H. Fei, X. Liu, Z. Li and W. Feng, *Electrochim. Acta*, 2015, **174**, 1088-1095.

S13 S. Maiti, A. Pramanik, U. Manju and S. Mahanty, *Micropor. Mesopor. Mat.*, 2016, **226**, 353-359.

S14 C. Shi, Q. Xia, X. Xue, Q. Liu and H. Liu, *RSC Adv.*, 2016, **6**, 4442-4447.